



The Influence of River Plume Discharge and Winds on Sediment Transport into a Coastal Mangrove Environment

Hemanth Vundavilli^{1,2} · Julia C. Mullarney¹ · Iain T. MacDonald³

Received: 6 June 2022 / Revised: 12 April 2024 / Accepted: 18 April 2024
© The Author(s) 2024

Abstract

We investigate how the physical forcing factors of river discharge and winds affect sediment delivery to, and retention within, mangrove-lined coastal regions. We use an idealized numerical model, broadly similar to the Firth of Thames deltaic system in New Zealand, to isolate and explore the underlying processes without some of the complexities of the real system. Total sediment transport and the relative contributions of riverine and bed-sourced sediment into the forest are assessed using a transect along the edge of the forest region. The model results demonstrate that both river discharge and winds alter the distribution of sediment transport, and that the spatial patterns relate to different regions of the river plume. At the river mouth (the near-field region), irrespective of the discharge employed, sediment fluxes are directed into the mangrove forest, indicating an accretionary environment consistent with satellite observations. Here, contributions from the riverine and bed-sourced sediments are similar. For small to medium discharge scenarios (up to $\sim 280 \text{ m}^3 \text{ s}^{-1}$, flow speeds $\sim 0.6 \text{ m s}^{-1}$), mass loads increase with river discharge. However, in the case of large discharge events, the high momentum in the near-field region allows the river plume to effectively transport sediment through the full width of forested region and out of the forest front. In the mid- and far-field regions of the plume, tidal influences also play a stronger role. Suspended sediment is primarily composed of bed-sourced material and transported out of the forest. Weaker winds are found to affect the far- and mid-field regions of the river plume. Stronger winds are able to reshape the entire plume structure, also including the near-field, such that sediment deposition is enhanced when winds are directed towards the forest.

Keywords River plumes · Mangrove vegetation · Delft3D · Discharge · Winds · Sediment transport · Sediment fluxes · Firth of Thames

Introduction

Mangroves are often the predominant vegetation growing along the coastlines in tropical and subtropical regions. In addition to providing valuable ecosystem services (e.g., Barbier et al. 2011; Sheaves et al. 2015), these salt-tolerant trees play a critical role in the morphological evolution of rivers, estuaries, and tidal environments. With extensive growth in the intertidal zones, mangroves can influence hydrodynamics within the aquatic environments by altering velocity fields (Nepf 2012; Mullarney et al. 2017), generating small-scale turbulence (Furukawa and Wolanski 1996; Norris et al. 2019), attenuating wave energy (Furukawa and Wolanski 1996; Mazda et al. 2006; Henderson et al. 2017), and reducing storm surges (Montgomery et al. 2019). Interactions between flows and mangroves' aerial root systems have been shown to facilitate both the deposition and erosion of sediment

Communicated by David K. Ralston

✉ Hemanth Vundavilli
vvhemanth@lsu.edu

Julia C. Mullarney
julia.mullarney@waikato.ac.nz

Iain T. MacDonald
iain.macdonald@niwa.co.nz

¹ Coastal Marine Group, School of Science, University of Waikato, Hamilton 3240, New Zealand

² Department of Oceanography and Coastal Sciences, College of Coast and Environment, Louisiana State University, Baton Rouge, LA 70803, USA

³ National Institute of Water and Atmospheric Research, Gate 10, Hamilton 3216, New Zealand

(Woodroffe 1992; Norris et al. 2021; Temmerman et al. 2007) depending on environmental conditions and vegetation parameters such as stem spacing, densities and geometries (Nepf 2004; Li et al. 2014).

The small (sub-meter) scale spatial heterogeneity of the vegetation-induced turbulence and associated variability in sediment resuspension (Temmerman et al. 2007; Zong and Nepf 2012; Chen et al. 2012) has been shown to influence morphological characteristics at the estuary scale. Mangrove roots (pneumatophores) generate stem-scale turbulence through the processes of vortex shedding and generation of eddies (Norris et al. 2019). Using field observations from a wave-influenced mangrove coastline in the Mekong Delta, Norris et al. (2017) explored the relationships between the density of mangrove roots and enhanced turbulence at the forest fringe (the transition between mudflat and vegetated area). These relationships were found to act as a control on sediment size distributions, and larger-scale erosion and accretion regimes (Fricke et al. 2017; Mullarney et al. 2017).

Tidal asymmetry is one of the principal mechanisms that transport sediment through mangrove environments (Furukawa and Wolanski 1996) by creating an imbalance in maximum flow speeds owing to friction caused by vegetative drag. Mazda et al. (1995) previously explored the observed tidal asymmetry patterns and noted that greater ebb flow speeds in the vegetated fringe led to ebb dominance of the region. Numerical modeling also revealed that vegetation changes the tidal asymmetry and the shape of the cross-shore bottom profile, with denser vegetation developing a more convex profile (Bryan et al. 2017). Some vegetated coastal systems have shown the ability to trap sufficient sediment to keep pace with sea-level rise (Lovelock et al. 2015; Kumara et al. 2010; Walsh and Nitttrouer 2004). However, this capability depends strongly on the amount of sediment delivered to the system. As rivers form the primary mechanism of sediment input to coastlines (Nitttrouer et al. 1995), it is critical to elucidate how factors such as variable discharge and winds influence the interaction of river plumes with vegetation, and hence also affect the sediment transport and deposition patterns.

Vundavilli et al. (2021) used an idealized numerical model of a mangrove-lined river debouching into a coastal bay to examine momentum balances and sediment fluxes into the forest from the different plume regions. They found that the principal balance between the bottom shear stress (enhanced by vegetation) and baroclinic pressure gradient largely controlled the sediment deposition in the riverine sections of the domain. During flood tide, vertical advection and diffusion enhanced erosion in the fringe region. The longer duration of high water slack at the forest fringe region, pressure gradients, and inertial acceleration led to the advection of the suspended sediment into the forest, where deposition occurred. In the idealized setup with a river boundary located to the south of the

domain, sediment deposition was more prominent on the western than the eastern side of the model owing to the influence of Coriolis (Southern Hemisphere). During ebb tide, when the freshwater plume was at its maximum extent, the barotropic and baroclinic pressure gradients and the Coriolis acceleration resulted in large portions of the riverine sediment being delivered to the forest and mudflat regions. The magnitude of acceleration terms and changes in bed elevations were smaller in the mid-field region. Away from the river mouth, in the far-field region of the plume, a more substantial tidal influence led to sediment erosion (also observed in Chen et al. 2009). In the shallow forested regions, the presence of vegetative drag slows down the movement of sediment offshore and leads to an overall flood dominance. In this previous study, momentum balances were evaluated for a single river discharge, and the effects of wind forcing were not considered. While much previous work has demonstrated significant dynamical responses of plumes to wind stress (e.g., Chao 1988a, b), the associated effects on sediment transport are not yet fully explored.

Our study was motivated by observations from the Firth of Thames located to the south of the Hauraki Gulf, New Zealand, as described in the prior study by Vundavilli et al. (2021). Aerial photography from the 1950s revealed that the Firth of Thames was a sandy tidal flat with mangrove vegetation near the Waihou and Piako river mouths. However, contrary to the global decline in the mangrove extent from the 1970s (Giri et al. 2011), the mangrove coverage in the Firth of Thames has been expanding rapidly (Fig. 1c). This expansion of mangrove vegetation has been attributed to the sediment input associated with deforestation and land-use changes (Horstman et al. 2018). We use a highly idealized model of this system to isolate the influence of forcing factors of river discharge and wind (both speed and direction) on a sediment-laden freshwater river plume in a mangrove-fringed coastal region. We undertake a large number of model simulations (57 runs each for vegetated and non-vegetated simulations) to explore how varying river discharges and winds affect the resulting sediment deposition patterns.

The “**Methods**” section describes the numerical model scenarios, including model parameters and boundary conditions. In the “**Results**” section, we show the dependence of sediment fluxes into the forest on varying river flows and wind speeds and directions. Process dynamics and the implications for the morphological evolution are discussed in the “**Discussion**” section. Conclusions are presented in the “**Conclusions**” section.

Methods

Model Grid and Bathymetry

The idealized model was designed to have similar overall dimensions and bathymetry profile to the Firth of Thames

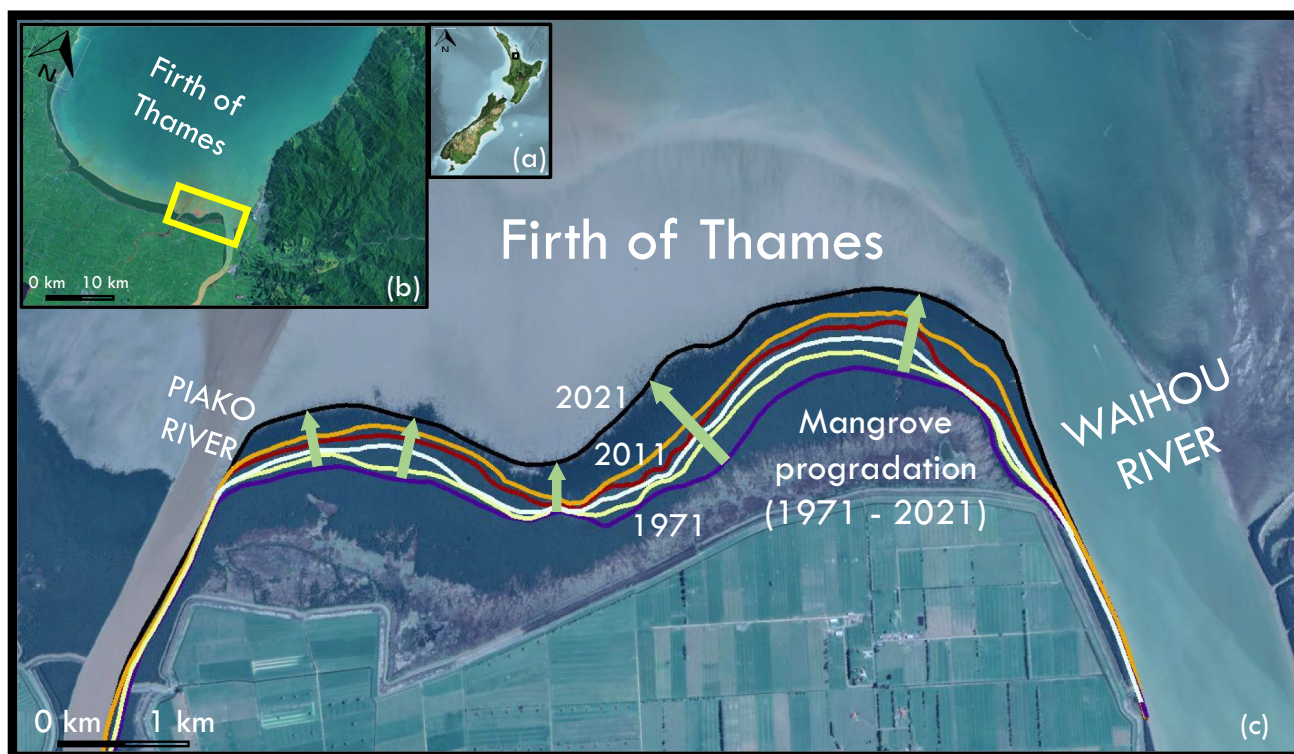


Fig. 1 Inset **a** Map of New Zealand and the location of Firth of Thames (thick black box). Panel **b** displays the location of the Waihou River (yellow rectangle). Panel **c** shows the mangrove progradation traced based on the Landsat imagery (1971–2021) obtained from the U.S. Geological Sur-

vey. Thick lines represent the extent of mangroves in 1971 (thick purple line), 1981 (thick light yellow), 1991 (thick white line), 2001 (thick red line), 2011 (thick orange line), and 2021 (thick black line). Thick green arrows represent the direction of mangrove progradation over time

(FoT, [S37°12' E175°30']) located to the south of the Hauraki Gulf, New Zealand, as described in the prior study by Vundavilli et al. (2021). However, a number of simplifications were made to the geometry and forcing of the real system. A 3-D curvilinear and symmetric (along the longitudinal axis) grid of 25 km in the longitudinal direction and 35 km in the latitudinal direction was decomposed into three model domains (Fig. 2a). The outer domain had a varying grid resolution of 500 m × 900 m near the tidal boundary to a finer grid size of 200 m × 475 m. The central domain covered the vegetated region and the tidal flats with grid cells of sizes ~ 218 m × 140 m in the deeper regions to 15 m × 6 m in the mangrove areas. Grid sizes in the lower domain consisting of the river varied from 25 m × 17 m at the river mouth to 15 m × 10 m at the upstream boundary. In the vertical direction, there were five sigma layers of equal thickness (20% of the water depth). A sensitivity analysis revealed that further refining the grid in either horizontal or vertical directions did not substantially alter results, and thus the above resolutions were used to minimize the computational time of simulations.

Numerical Model

The idealized numerical model used in this study was developed in Delft3D (Deltares 2021). The Delft3D software package solves both the continuity and the three-dimensional shallow-water equations under the Boussinesq assumption and has been successfully applied across many modeling studies to study morpho-hydrodynamics (Roelvink and Van Banning 1995; Lesser et al. 2004).

The presence of vegetation alters the flow fields and sediment balance through hydraulic resistance. Parameters such as stem density, thickness, and flexibility help determine this hydraulic resistance (Oorschot et al. 2016). In Delft3D-FLOW (Lesser et al. 2004), the directional point model (DPM) extends the one-dimensional vertical momentum equation and includes turbulent closures. The DPM represents vegetation as rigid vertical cylinders, accounting for stem height and density, to simulate vertical vegetative drag (Baptist 2005). Following reasoning by Horstman et al. (2013), we use a spatially varying bed roughness coefficient to reduce the computational time of our simulations.

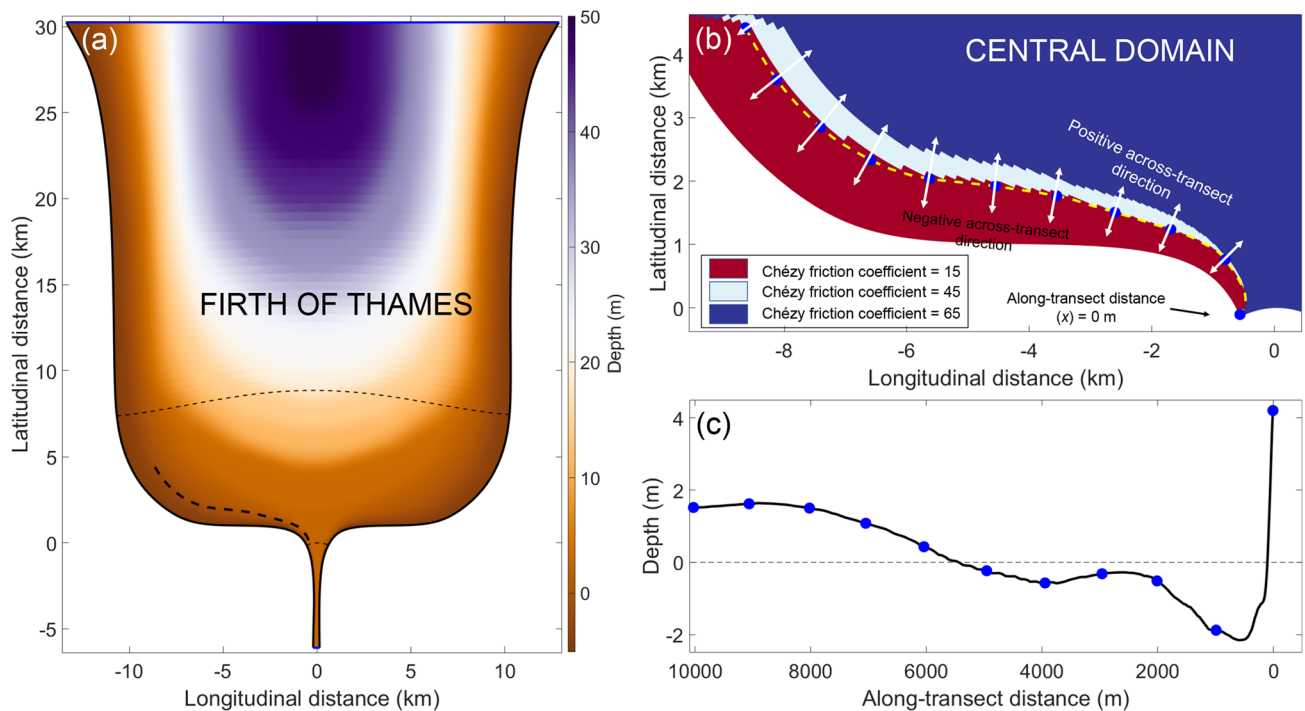


Fig. 2 Panel **a** shows the idealized symmetric bathymetry, transect along the forest edge (black dashed line), and the domain decomposed grid boundaries (thin black dashed lines), **b** spatially varying Chézy coefficient used in the model central domain to represent vegetation, and **c** shows the depth profile along the transect shown

in panel **(b)**. Thick blue lines in panel **(a)** represent tidal (top) and river (bottom) boundaries. The transect is shown by dashed black and dashed yellow lines in panels **(a)** and **(b)**, respectively. Blue circles are shown every 1000 m. In panel **(b)**, the white arrows depict the across-transect directions

In our vegetated simulations, a spatially varying Chézy value (Fig. 2b) was employed to represent vegetation based on literature values (Zhang et al. 2012; Mazda et al. 1997). In particular, the forest was represented with a Chézy value of $15 \text{ m}^{1/2} \text{ s}^{-1}$ (corresponding to a friction coefficient of $C_D = 0.044$) and the intertidal zone with a Chézy value of $65 \text{ m}^{1/2} \text{ s}^{-1}$ ($C_D = 0.0023$). The thin transition zone between the forest and intertidal flats ($\sim 200 \text{ m}$ fringe region) was represented with a value of $45 \text{ m}^{1/2} \text{ s}^{-1}$ ($C_D = 0.0048$).

Model Parameters and Boundary Conditions

The model was forced along the northern boundary with an M2 astronomic tide of amplitude 1.3 m and a constant salinity of 31 ppt. The southern river boundary was forced with a freshwater discharge with a riverine sediment input of 1 kg m^{-3} . The Coriolis parameter was defined for -37° latitude. The horizontal eddy viscosity and diffusivity were set to $1 \text{ m}^2 \text{ s}^{-1}$, and $0.1 \text{ m}^2 \text{ s}^{-1}$, respectively. The settling velocity, critical bed shear stress, and erosion parameters were set at 0.5 mm s^{-1} , 0.1 N m^{-2} , and $0.0001 \text{ kg m}^{-2} \text{ s}^{-1}$, respectively, based on literature values (Mehta and Partheniades 1982) representative of a

cohesive sedimentary environment. In our model runs with winds, spatially uniform wind speeds and directions were specified over the entire domain. All the wind parameters, such as air density and drag coefficients, were set to Delft3D defaults (Deltares 2021). Models used a threshold depth of 0.1 m, and a cyclic advection scheme was chosen for the spatial discretization of momentum.

To satisfy the Courant-Friedrichs-Lewy condition, a time step of 0.01 min was used. The model simulation was forced at the river boundary with a freshwater discharge (no sediment input) for an initial spin-up period of 7 days (flow time) to achieve a quasi-steady state. Subsequently, the model simulations were conducted for another seven days with a sediment concentration input of 1 kg m^{-3} through the river boundary. This approach allowed us to track the delivery of sediment to the mangrove forest. While the sediment class was restricted to cohesive sediments in our model simulations, we labeled the sediments to distinguish between the riverine (new sediments input at the boundary) and bed-sourced sediments (legacy sediments). Following sensitivity analysis, a layered bed stratigraphy was incorporated into the model with 100 layers of 2.5 cm thickness.

Modeled Scenarios

River discharges were selected to encompass the range observed over a 40-year time series (1981–2022) recorded for the Waihou River at an upstream station. The discharge was varied from $0 \text{ m}^3 \text{ s}^{-1}$ to $480 \text{ m}^3 \text{ s}^{-1}$ (largest observed), with an increment of $35 \text{ m}^3 \text{ s}^{-1}$ (Table 1). Additional runs with winds were applied for three different discharges ($35 \text{ m}^3 \text{ s}^{-1}$, $175 \text{ m}^3 \text{ s}^{-1}$, and $480 \text{ m}^3 \text{ s}^{-1}$). Winds directions varied from 0 to 360° with increments of 45° , and speeds of 5 m s^{-1} and 10 m s^{-1} , noting that 5 m s^{-1} was the mean wind speed recorded by a nearby climate station over the period (2019–2020).

Analysis of Model Results

Previous studies have extensively reported the edge of the forest (mangrove fringe) as a highly dynamic region (Mullarney et al. 2017). Within mangrove environments, feedback between sediment transport and mangroves at a small scale plays a crucial role in altering the large-scale dynamics of the region (Balke et al. 2011, 2013; Wolanski et al. 2002). In our model, to quantify the sediment transport into the vegetation, we define a transect which separates the forest from the mudflat along the edge of the west-side mangrove forest (Fig. 2c). Note that depth varies along the transect. The transect begins from the raised river bank located in the river mouth, incorporates a slightly deeper section of the mudflat around the bend, and extends along the edge of the western mangrove forest. The depth profile along the transect is shown in Fig. 2c, and the along-transect position $x = 0 \text{ m}$ corresponds to the beginning of the transect. A few regions close to the river mouth ($0 \lesssim x \lesssim 100 \text{ m}$) and shallow regions away from the river mouth ($x \gtrsim 6000 \text{ m}$) remained dry throughout the model simulations.

Sediment Flux Calculations

In order to investigate the critical linkages between the riverine flows, tidal influence, and the wind in the presence of

vegetation, we evaluate the sediment fluxes for sediment sources (riverine and bed-sourced) separately. Instantaneous sediment fluxes for each type of sediment source (Q , $\text{kg m}^{-1} \text{ s}^{-1}$) at time t , in the across-transect direction, are obtained by integrating the product of sediment concentration and the horizontal across-transect velocity over the height of water column:

$$Q(t) = \int_0^{h(t)} c(t, z) \cdot v(t, z) \cdot dz, \quad (1)$$

where $c(t, z)$ is the instantaneous sediment concentration (kg m^{-3}), $v(t, z)$ indicates the horizontal across-transect velocity at height z and time t , and h is the height of the water column. The fluxes are integrated over the ebb, flood, and the full tidal cycle to provide the net sediment transport into and out of the forest region. In the intertidal zones, only the timesteps when the grid cell was fully inundated were used in the flux calculations.

The time-integrated fluxes (kg m^{-1}) were further integrated along the entire length of the transect (Eq. 2) to estimate the net mass transfer (kg),

$$M = \int_0^X Q \cdot dx, \quad (2)$$

where X is the total length of the transect in the along-transect direction.

In our evaluations, positive fluxes correspond to an off-shore flux directed out of the mangrove forest, and negative fluxes correspond to sediment movement into the mangrove forest (Fig. 2b).

Results

As this study aims to understand the morphological response to sediment transported in the buoyant river plume under the influence of varying river flows and winds, we briefly describe the plume hydrodynamics but predominantly focus

Table 1 Model simulations undertaken in our study for the vegetated simulations. Simulations 58–114 used a uniform Chezy roughness coefficient of $65 \text{ m}^{1/2} \text{ s}^{-1}$ ($C_D = 0.0023$) throughout the domains, but were otherwise identical to 1–57

Varying parameters	Model runs~	River discharge ($\text{m}^3 \text{ s}^{-1}$)	Wind speed (m s^{-1})	Wind direction ($^\circ$)	Increment in wind direction
River discharge	1–15	0, 35, 70, 105, 140, 175, 210, 245, 280, 315, 350, 385, 420, 455, 480	0	-	-
Winds	16–22	35	5	0–315	45°
	23–29	35	10	0–315	45°
	30–36	175	5	0–315	45°
	37–43	175	10	0–315	45°
	44–50	480	5	0–315	45°
	51–57	480	10	0–315	45°

on the sediment transport results. A detailed description of the model output from a single discharge scenario without winds, including an analysis of surface and bottom layer momentum balances within various regions of the river plume, can be found in Vundavilli et al. (2021).

Plume Dynamics

Tidal residual velocities were evaluated at the river mouth (latitudinal distance of ~ 1 km, Fig. 2a) for each discharge scenario undertaken in our study. In the $35 \text{ m}^3 \text{ s}^{-1}$ discharge scenario, tidal residual velocities ranged from 0.2 m s^{-1} on the surface layer to 0.06 m s^{-1} on the bottom layer. In the large discharge scenario ($480 \text{ m}^3 \text{ s}^{-1}$), these velocities were 1.2 m s^{-1} and 0.45 m s^{-1} on the surface and bottom layers, respectively.

An example of along-transect distributions of residual across-transect velocities, riverine sediment concentrations, and across-transect horizontal sediment fluxes is shown in Fig. 3 for the simulation with a river flow of $175 \text{ m}^3 \text{ s}^{-1}$. We divide the transect into three zones to highlight the different sections of the river plume which interact with the vegetation at these locations. Following Hetland (2005), these distinct dynamical regions of the river plume in our model simulations are the near-field mixing zone, which was localized

at lower salinity values (5–15 ppt), mid-field region, which encapsulated the anticyclonic bulge (16–25 ppt), and the far-field which had a lower rate of mixing with a salinity range of 26–31 ppt.

While these salinity ranges are approximate, the isohaline-based approach offers a convenient method to categorize the results into regions with distinct dynamics. These areas align closely with findings from (Horner-Devine et al. 2015, their Fig. 2), and different regions evaluated from the momentum balances (Vundavilli et al. 2021). In the near-field, dynamics are primarily driven by advection and shear mixing (McCabe et al. 2008), contrasting with the far-field where flows are heavily influenced by tidal currents, winds, and Coriolis effects (Horner-Devine et al. 2015; Mazzini and Chant 2016). Additionally, the transitional mid-field region marks the point where the river plume enters coastal waters, undergoing a shift from an inertial near-field jet to a geostrophic or wind-dominated far-field plume, with Earth's rotation playing a significant role in the plume dynamics (Garvine 1987).

For example, in the model scenario with $175 \text{ m}^3 \text{ s}^{-1}$ discharge, mean across-transect horizontal velocities along the transect over ebb ranged from $\sim -0.12 \text{ m s}^{-1}$ in the near-field zone close to the river mouth ($100 \text{ m} \lesssim x \lesssim 2100 \text{ m}$) to about $\sim 0.03 \text{ m s}^{-1}$ in the near-bed region of the mid-field zone

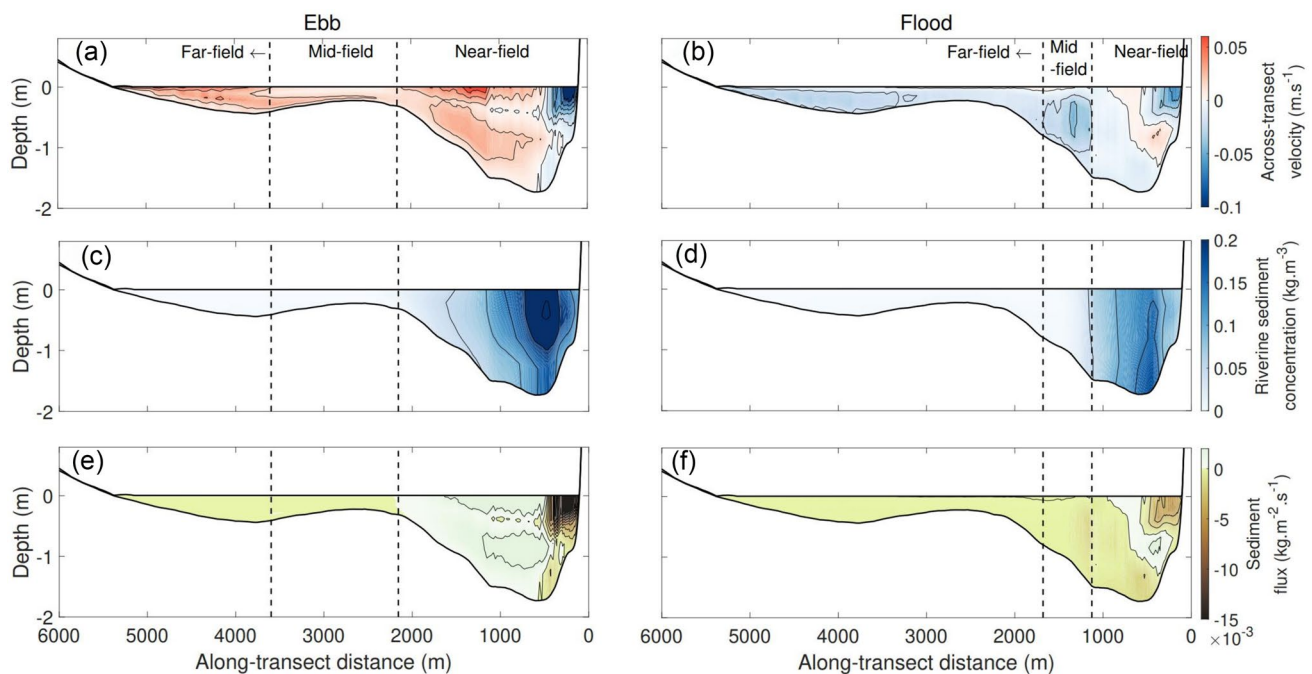


Fig. 3 Across-transect velocity (a, b), riverine sediment concentration (c, d), and across-transect horizontal sediment flux (e, f) along the transect for the $175 \text{ m}^3 \text{ s}^{-1}$ discharge scenario (Run 6, Table 1). Panels a, c, and e are mean over ebb and panels b, d, and f are mean over the flood tide. The across-transect distance of zero corresponds

to the shallow river bank. Dashed black lines delineate the different regions relative to the sediment plume. Thin black lines show 0.02 m s^{-1} , 0.05 kg m^{-3} , and $0.002 \text{ kg m}^{-2} \text{ s}^{-1}$ contours in panels a and b, c and d, and e and f, respectively

($2100 \text{ m} \lesssim x \lesssim 3500 \text{ m}$) and far-field zones ($x \gtrsim 3500 \text{ m}$). While across-transect velocities were directed into the forest zone in the near-field region (negative), in the mid- and far-field regions, velocities were oriented out of the forest (positive). Over ebb, as the plume debouched from the river mouth, riverine sediment remained in the surface layer and underwent rapid mixing in the near-field zone. The sediment concentrations ranged from $\sim 0.25 \text{ kg m}^{-3}$ at the surface to $\sim 0.15 \text{ kg m}^{-3}$ at the bottom. In the mid-field and far-field zones, riverine sediment concentrations were close to zero.

Over the flood tide, as the plume was pushed back into the river mouth due to the incoming tidal currents, the near-field zone extended just over $\sim 1000 \text{ m}$ of the transect ($100 \text{ m} \lesssim x \lesssim 1100 \text{ m}$), and the mid-field region was also narrower ($1100 \text{ m} \lesssim x \lesssim 1600 \text{ m}$). In the far-field region of the river plume ($x \gtrsim 1100 \text{ m}$), as the plume lost its momentum, tidal currents dictated the transport of the sediment, and the across-transect velocities were directed into the forest (Fig. 3b).

In general, during the flood stage, the maximum contribution of the riverine sediment occurred within $\sim 0.5 \text{ m}$ from the bed (Fig. 3d). Magnitudes of the across-transect mean velocities ranged from $\sim 0.02 \text{ m s}^{-1}$ in the surface to $\sim 0.004 \text{ m s}^{-1}$ in the bottom layer. While the surface layer velocities were directed out of the forest, the bottom layer velocities were directed into the forest region (Fig. 3b). In the near-field region ($100 \text{ m} \lesssim x \lesssim 1100 \text{ m}$), modeled riverine sediment concentrations in the bottom were ~ 5 times greater than in the surface layer (Fig. 3d). Away from the river mouth in the far-field region of the river plume, river-sourced sediment concentrations were negligible. Along the transect, over the flood stage of the tidal cycle, in the near-field zone ($100 \text{ m} \lesssim x \lesssim 1100 \text{ m}$), the vertical sediment fluxes were directed into the forest region in the surface layer and away from the forest in the bottom layer (Fig. 3f).

Tidally Integrated Fluxes

The depth-integrated across-transect fluxes of riverine, bed-sourced and the total sediment for the $175 \text{ m}^3 \text{ s}^{-1}$ discharge scenario are shown in Fig. 4. For along-transect distances of $x \gtrsim 2500$, fluxes were $\mathcal{O}(0)$, so only the regions close to the river mouth are shown in subsequent figures. Over the ebb stage (Fig. 4b), in the regions closer to the river mouth ($100 \text{ m} \lesssim x \lesssim 500 \text{ m}$), both the riverine and bed-sourced sediment fluxes were found to be directed into the forest region with magnitudes of the riverine sediment fluxes nearly double that of the bed-sourced sediment fluxes. Farther along the transect ($500 \text{ m} \lesssim x \lesssim 1100 \text{ m}$), as the river pushed through the transect owing to the near-field circulation, the direction of the fluxes was reversed, and sediment was directed out of the forest region (Fig. 4b). Riverine sediment

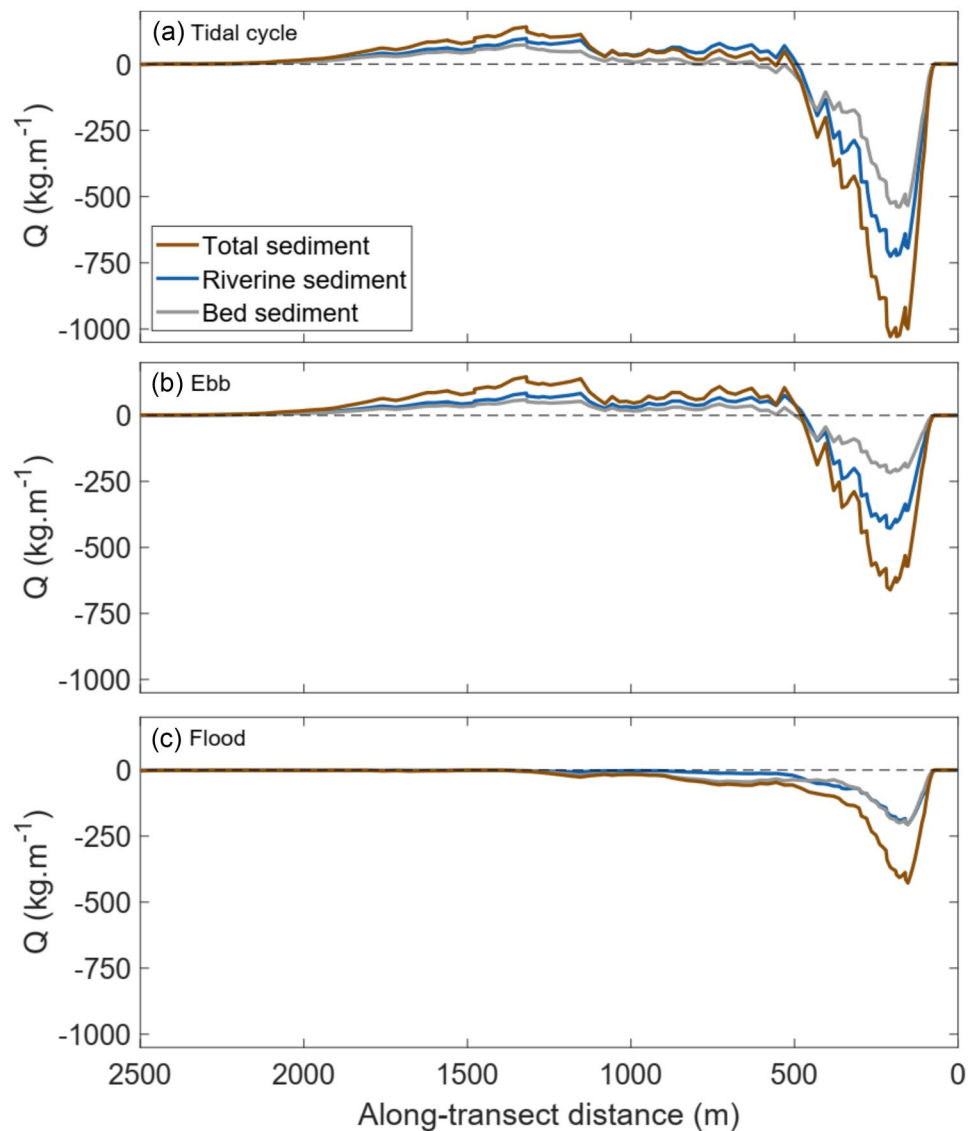
transport remained the dominant contributor to sediment transport in this part of the transect. In the far-field region ($x \gtrsim 1100 \text{ m}$), owing to the loss of momentum carried by the river in this region, tidal currents remained the major drivers of the sediment, and both the riverine and bed-sourced sediment were directed out of the forest (Fig. 4b). As expected, the bed-sourced sediment dominated contributions towards the total transport, with only modest contributions from the riverine sediment.

Over the flood tide, sediment fluxes were directed into the forest region close to the entirety of the transect; however, the dominant contributors to the fluxes varied along the transect (Fig. 4c). Riverine and bed-sourced sediments were of similar magnitudes contributions in the near-field region of the river plume ($0 \text{ m} \lesssim x \lesssim 500 \text{ m}$); however, as the freshwater plume was pushed back into the river mouth due to the oncoming tidal currents, the plume spread was restricted, and bed-sourced forms the largest contributor to the fluxes elsewhere along the transect (Fig. 4c). Over the full tidal cycle, sediment was transported into the forest close to the river mouth ($100 \text{ m} \lesssim x \lesssim 500 \text{ m}$), with greater riverine sediment contributions over that of the bed-sourced sediment by nearly $\sim 45\%$. Farther along the transect ($500 \text{ m} \lesssim x \lesssim 1000 \text{ m}$), the total sediment transport was directed out of the forest as the river sediment entered the forest in the near-field zone, and the presence of strong river momentum helped transport/advection this sediment through the forest front onto the mudflat region close to the river mouth (Fig. 4b). While directional trends remained similar for both the vegetated and non-vegetated runs, the total, river, and bed-sourced sediment flux magnitudes were larger in the case of non-vegetated due to lack of vegetative drag and faster flow velocities in both the near- and mid-field regions of the river plume. However, in the far-field region, bed-sourced sediment fluxes were found to be larger in the case of vegetated simulations, in comparison to non-vegetated simulations as a result of the vegetation drag reducing flow velocities.

Tidally Integrated Fluxes and Total Sediment Mass Loads Under Varying River Flows

To explore the impact of different discharges, we analyzed sediment fluxes along the transect (Fig. 5a) and total sediment mass loads integrated across the entire length of the transect (Fig. 6). Close to the river mouth, sediment was transported into the forest lining the river banks, and total sediment flux magnitudes increased with discharge. The relative importance of the sediment source varied across river discharges. In particular, for low to medium river flows ($35 \text{ m}^3 \text{ s}^{-1}$ – $210 \text{ m}^3 \text{ s}^{-1}$), the contributions of riverine and bed-sourced sediment were similar in the near-field

Fig. 4 Across-transect total, riverine, and bed-sourced sediment fluxes (Q) along the transect were evaluated for the $175 \text{ m}^3 \text{ s}^{-1}$ discharge scenario integrated over: **a** the full tidal cycle, **b** the ebb stage, and **c** the flood stage. Thick brown lines represent the total sediment fluxes, blue lines represent the riverine sediment fluxes, and thick gray lines represent the corresponding fluxes for the bed-sourced sediment. In our evaluations, positive and negative fluxes indicate sediment transport out of the forest and into the forest region, respectively

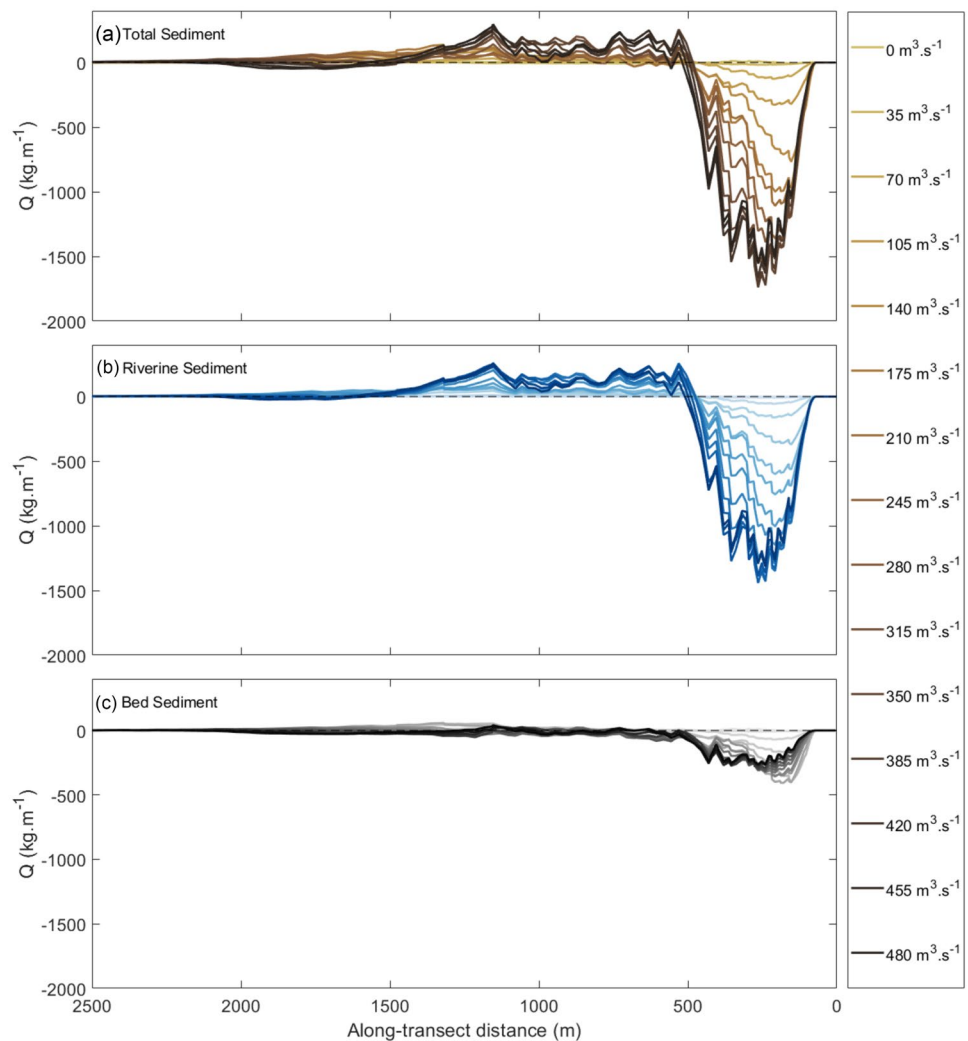


region of the river plume. For higher river flows, the riverine sediment was the major contributor towards the total sediment into the forest in the region ($0 \lesssim x \lesssim 500 \text{ m}$, Fig. 5a). In the region ($500 \text{ m} \lesssim x \lesssim 1000 \text{ m}$), the riverine sediment transport was directed out of the forest irrespective of the discharge employed in our model simulations. Farther away from the river mouth, in the region, $x \gtrsim 1500 \text{ m}$, the total sediment transport was directed out of the forest region for all except the highest discharges. For the very large discharges ($> 210 \text{ m}^3 \text{ s}^{-1}$), the anticyclonic bulge of the river plume extended into this region and moved suspended bed-sourced sediment (lifted off during flood) into the forest (Fig. 6a and c).

The total, riverine, and bed-sourced sediment mass loads integrated along the entire transect for the different discharges are shown in Fig. 6. The transport over the flood stage of the

tidal cycle was an order of magnitude larger than that during the ebb and hence dominated the contributions to the total transport. The total sediment mass load was directed into the forest for all discharges, indicating an accretionary environment. Mass loads were found to increase approximately linearly with discharge across the range $70 \text{ m}^3 \text{ s}^{-1}$ to $280 \text{ m}^3 \text{ s}^{-1}$, at which point, further increases in discharge only resulted in small amounts of additional sediment being delivered to the forest. For these larger discharges, sediment delivered to the mangroves was pushed through and out of the forest owing to high river momentum (Fig. 5b). The relative contributions towards the total sediment mass loads were found to be similar for both the bed-sourced and riverine sediment for river discharges up to $210 \text{ m}^3 \text{ s}^{-1}$, beyond which the relative contribution of the riverine sediment increased (to approximately double that of the bed-sourced sediment).

Fig. 5 Comparison of the tidal integrated across-transect **a** total sediment fluxes (brown lines), **b** riverine sediment fluxes (blue lines), and **c** bed-sourced sediment fluxes (black lines) for each of the discharge scenarios (Table 1, row 1) undertaken in the study. Colors show individual discharge scenarios from low discharge (lighter shades) to high discharge (darker shades). In our evaluations, positive and negative fluxes indicate sediment transport out of the forest and into the forest region, respectively



Response of the River Plume and Sediment Transport to Varying Wind Velocities

Influence of Winds on the Plume Structure

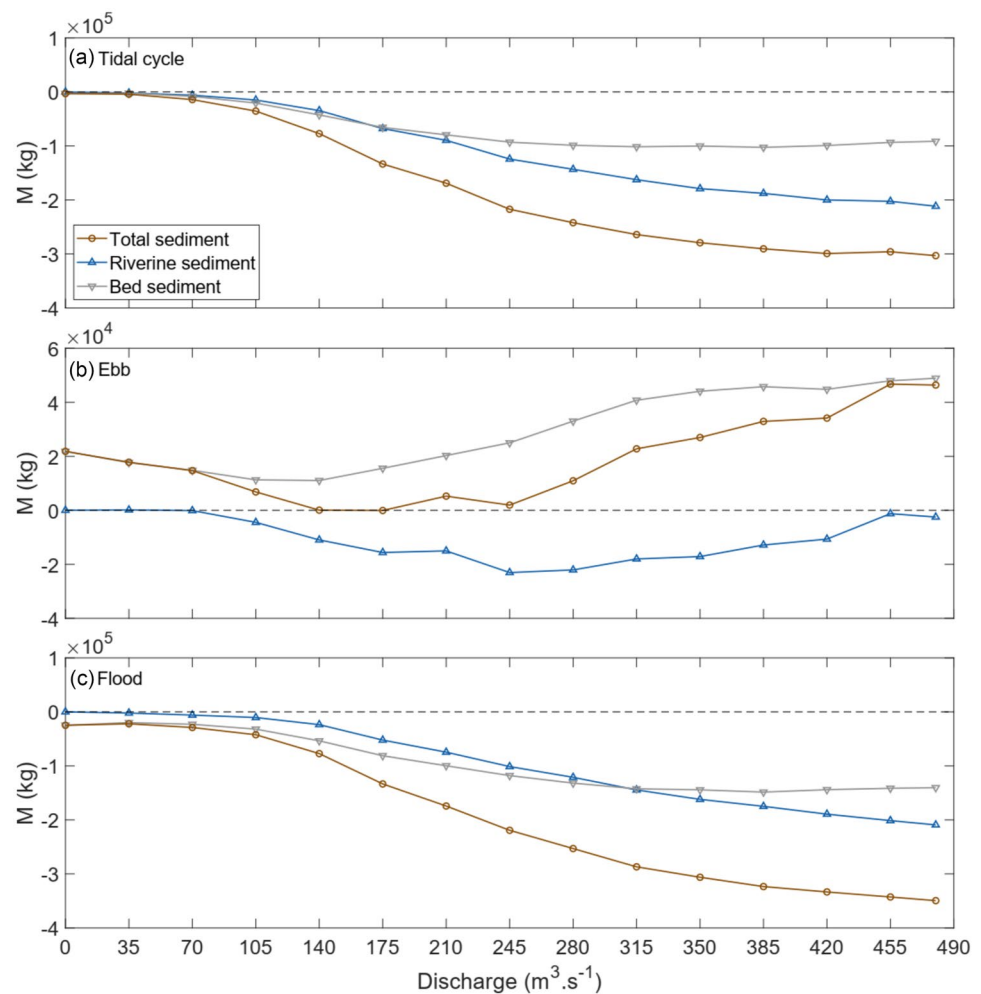
The influence of wind direction on the sediment transport could be seen in the tidal residual of the riverine sediment concentrations and horizontal velocities in the surface layer (Fig. 7 provides an example for wind speeds of 5 m s^{-1} and a discharge of $175 \text{ m}^3 \text{ s}^{-1}$). Compared with the no-wind scenario (Fig. 7a), northerly winds pushed the plume back into the river mouth, accumulating the riverine sediment in the near-field region. While the surface current residuals remained unaltered in this region ($0 \lesssim y \lesssim 2 \text{ km}$ in the latitudinal direction), residual currents in the region away from the river mouth ($x \geq 2 \text{ km}$ in the longitudinal direction) were altered due to the surface winds.

Across all of the model simulations, easterly winds (90°) were found to have maximized the sediment transport into the transect (Fig. 7d). Southerly winds (180°) effectively increased the overall plume extent in our simulations and increased the sediment concentration observed close to the river mouth ($\sim 0.2 \text{ kg m}^{-3}$). Westerly, south-westerly, and north-westerly winds were sufficient to dominate over Coriolis and generate a strong wind-driven eastward flow in the regions away from the river mouth (Fig. 7g, h, and i).

Tidally Integrated Fluxes Under Varying Winds

The total sediment flux, riverine sediment flux, and bed-sourced sediment fluxes along the transect evaluated over a tidal cycle for a $175 \text{ m}^3 \text{ s}^{-1}$ discharge with varying wind

Fig. 6 Comparison of the sediment mass loads (in kg) of total (brown lines), riverine (blue lines), and bed-sourced sediment (gray lines) through the transect as a function of each discharge scenario undertaken in the study. Panels **a**, **b**, and **c** show the mass loads integrated over the entire tide, ebb stage, and flood stages of a tidal cycle, respectively. Note the different y-axis scales in panels (a), (b), and (c). Positive and negative mass loads indicate sediment transport out of the forest and into the forest region, respectively



directions and two wind speeds (model runs 16–57, Table 1) are shown in Fig. 8.

The response of the plume to the winds differed between the regions of the sediment plume along the transect. Wind speeds of 5 m s^{-1} were insufficient to alter the sediment transport direction closer to the river mouth. In the region close to the river mouth ($0 \lesssim x \lesssim 500 \text{ m}$), total sediment transport was found to be directed into the forest irrespective of the direction of the wind, with both riverine and bed-sourced sediments contributing to the total sediment transport (Fig. 8a). Farther along the transect ($x \gtrsim 500 \text{ m}$), total sediment transport in this region was dictated by the wind direction. In particular, in the case of easterly wind directions (0° – 180°), the total sediment transport was directed into the forest; however, in the case of westerly wind directions (225° – 315°), the sediment transport was instead directed out of the forest.

In our model simulations, the presence of strong winds (10 m s^{-1} , Fig. 8b, d, and f) significantly altered the total transport fluxes along the transect. Close to the river mouth

($0 \lesssim x \lesssim 500 \text{ m}$), while the total sediment transport was directed into the forest irrespective of the wind direction, the magnitudes increased by nearly 75% in the case of easterly winds and reduced by 42% in the case of westerly directions (225° , 270° , 315° , Fig. 8b) in comparison to that of 5 m s^{-1} wind speeds. In the region defined by the along-transect distance of $500 \text{ m} \lesssim x \lesssim 1500 \text{ m}$, as the wind altered the plume structure, magnitudes of the total sediment fluxes were largest (due to larger riverine and bed-sourced sediment contributions) in the case of easterly wind directions, while conversely, fluxes were smaller for westerly wind directions. Similarly, in the far-field region of the plume where the influence of river momentum was minimal, winds controlled the direction of the total sediment transport flux (Fig. 8a). In the case of westerly winds, the entirety of the sediment plume was pushed away from the western mangrove forest, and hence contributions of the riverine sediment fluxes towards the total transport were negligible.

Interestingly, along the forest in the region ($x \gtrsim 1500 \text{ m}$), the bed-sourced sediment fluxes in the presence of 5 m s^{-1}

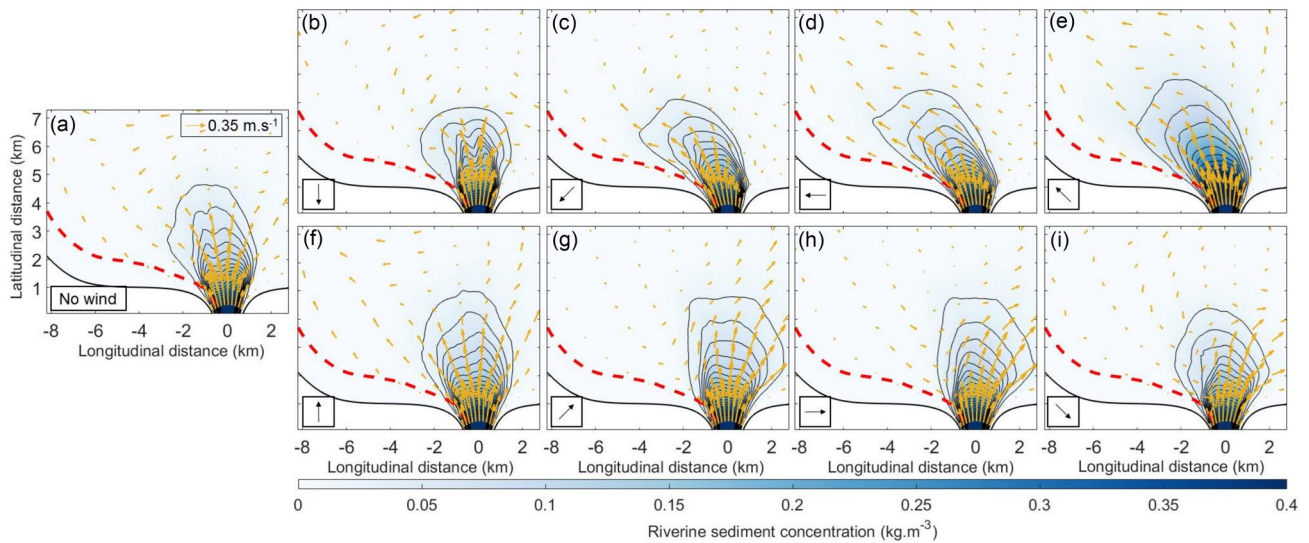


Fig. 7 Response of the surface layer tidal residual sediment plume with discharge forcing of $175 \text{ m}^3 \text{ s}^{-1}$ and 5 m s^{-1} wind speeds compared to **a** no-wind scenario corresponding to model run 6 (Table 1), **b** northerly wind direction (0°), **c** northeasterly wind direction (45°), **d** easterly wind direction (90°), **e** southeasterly wind direction (135°), **f** southerly wind direction (180°), **g** southwesterly wind direction

(225°), **h** westerly wind direction (270°), and **i** northwesterly wind direction (315°). Yellow arrows represent the surface layer residual velocities. The thick red line shows the location of the transect. Colorbar represents riverine sediment concentration in kg m^{-3} . Contour intervals are 0.02 kg m^{-3}

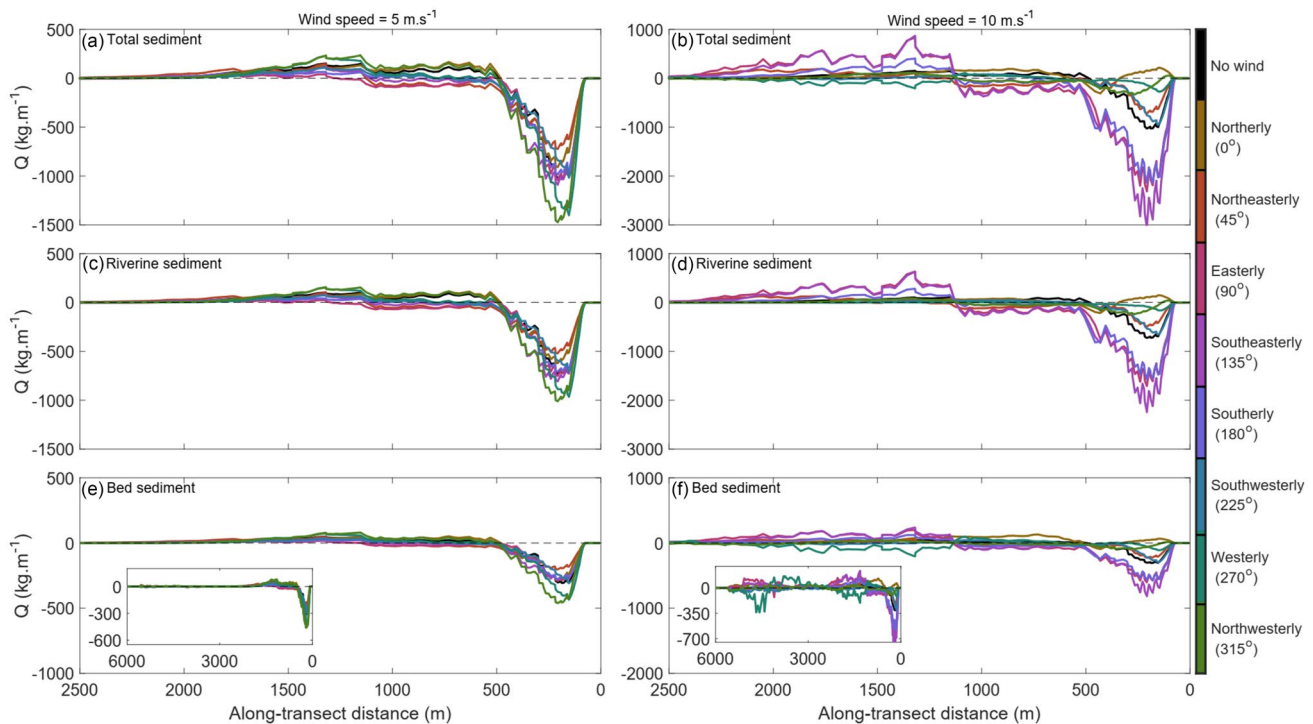


Fig. 8 Integrated across-transect fluxes for the river discharge scenario of $175 \text{ m}^3 \text{ s}^{-1}$, for wind speeds of 5 m s^{-1} (left-hand panels), and 10 m s^{-1} (right-hand panels) for different wind directions. Panels **a** and **b** are total sediment fluxes, panels **c** and **d** are fluxes of river-

ine sediments, and panels **e** and **f** are bed-sourced sediments. In our evaluations, positive and negative fluxes indicate sediment transport out of the forest and into the forest region, respectively

winds were insignificant; however, strong winds of 10 m s^{-1} significantly altered the bed-sourced sediment fluxes (lower left inset (Fig. 8e and f)). In particular, while the bed-sourced sediments were $\sim 10\%$ of that observed in the near-field region, in the case of light winds of 5 m s^{-1} , bed-sourced sediments were $\sim 33\%$ in the case of 10 m s^{-1} wind speeds.

During flood, magnitudes of bed-shear stress were larger in the case of stronger winds (10 m s^{-1}) for all wind directions except the northerly wind direction. This enhanced bed-shear stress during the flood stage of the tidal cycle can explain the dominant contribution of bed-sourced sediment to the total sediment transport, as the sediment is lifted into suspension due to the winds as well as the oncoming tidal currents. In the case of the northerly wind direction, the reduced bed shear stress (in the case of 10 m s^{-1}) can be explained by the reduced water depth as the plume is pushed back into the river strongly in the presence of oncoming tidal currents and the strong winds.

During ebb, as the plume debouches into the model domain, the magnitudes of bed shear stress were well below the critical bed-shear stress in the case of 5 m s^{-1} wind velocities. These low magnitudes can help explain the low contributions of bed-sourced sediment towards the total sediment mass loads modeled in our study. Conversely, in the case of strong winds during ebb, wind stress is sufficient to enhance the bed shear stress in the region, which in turn, increases the contribution of bed-source sediment towards the total mass loads modeled.

In our model simulations, the extent of the wind influence on the type of sediment source varied with distance from the river mouth. Closer to the river mouth (near-field region), maximum fluxes of riverine sediments into the forest varied between $\sim 500 \text{ kg m}^{-1}$ and $\sim 750 \text{ kg m}^{-1}$ for all the wind directions; however, the bed-sourced sediment ranged from $\sim 200 \text{ kg m}^{-1}$ and $\sim 650 \text{ kg m}^{-1}$. In the scenarios with stronger wind speeds (10 m s^{-1}), this variability is further enhanced (Fig. 8d and f). Interestingly, farther away from the river mouth in the mid-field region of the river plume, while the weaker winds (speeds of 5 m s^{-1}) introduced similar variabilities within riverine and bed-sourced sediment, stronger winds increased the variability for the bed-sourced sediment. This anomaly can be attributed to enhanced bed-shear stresses within the mid-field region due to stronger winds and shallower water depths.

The Combined Influences of Discharge and Winds on Tidally Integrated Sediment Mass Loads

The combined effects of discharge and winds on the mass loads into the forest over a tidal cycle are summarized in Fig. 9. In the presence of 5 m s^{-1} wind speeds, total

sediment mass loads were found to be directed into the forest irrespective of the wind direction. However, in the case of low-medium river flow events ($35 \text{ m}^3 \text{ s}^{-1}$ and $175 \text{ m}^3 \text{ s}^{-1}$), total sediment mass loads were larger for all the easterly wind directions (45° – 135°). On the contrary, northerly, southerly, and westerly wind speeds of 10 m s^{-1} were sufficient to alter the total sediment transport mass loads in the case of both the $35 \text{ m}^3 \text{ s}^{-1}$ and $175 \text{ m}^3 \text{ s}^{-1}$ discharge scenarios. While the largest magnitudes were observed in the southeasterly wind scenario, the lowest mass loads were found to be in the case of 0° for both cases of river discharge.

In the presence of 5 m s^{-1} wind speeds, mass loads varied substantially with wind direction for the high riverine discharge ($480 \text{ m}^3 \text{ s}^{-1}$) scenario. Interestingly, the largest sediment mass load was recorded in the south-westerly wind scenario (225° , a westerly wind direction that directed the sediment plume away from the transect). This anomaly can be attributed to the decreased river sediment transport outflow (compared to remaining wind directions) in the mid-field region of the sediment plume (Fig. 8c, $1500 \text{ m} \lesssim x \lesssim 2100 \text{ m}$), which consequently led to higher mass loads into the forest. In the presence of 5 m s^{-1} wind speeds, both the riverine and bed-sediment mass loads were directed into the transect for all the discharge scenarios irrespective of the wind direction, except the model run with $480 \text{ m}^3 \text{ s}^{-1}$ in the case of northerly winds where the total sediment mass loads were instead directed out of the forest (Fig. 9c). The reversal of the plume into the river due to wind can explain this reversal of the sediment transport direction. However, as the contribution of bed sediment transport was significantly lower than that of the riverine sediment, the sediment transport was found to be directed into the forest.

In the presence of strong winds (10 m s^{-1}), the sediment mass loads were approximately double those in the 5 m s^{-1} wind speed cases. Total mass loads increased non-linearly with discharge: Compared to the $35 \text{ m}^3 \text{ s}^{-1}$ discharge scenario, mass loads were ~ 10 and 15 times larger for the $175 \text{ m}^3 \text{ s}^{-1}$ and $480 \text{ m}^3 \text{ s}^{-1}$ discharge scenarios, respectively. The dependence on wind direction was more pronounced and similar for the larger discharges, with the notable result that irrespective of discharge, for northerly winds, sediment transport was directed out of the forest. The maximum mass loads were directed into the forest under southeasterly winds for larger river flows. Additionally, while the riverine sediment transport dominated the total sediment transport in the case of $175 \text{ m}^3 \text{ s}^{-1}$ and $480 \text{ m}^3 \text{ s}^{-1}$ discharges, bed-sourced sediment remained the major contributor towards the total sediment transport for all the wind directions employed in the case of $35 \text{ m}^3 \text{ s}^{-1}$ discharge.

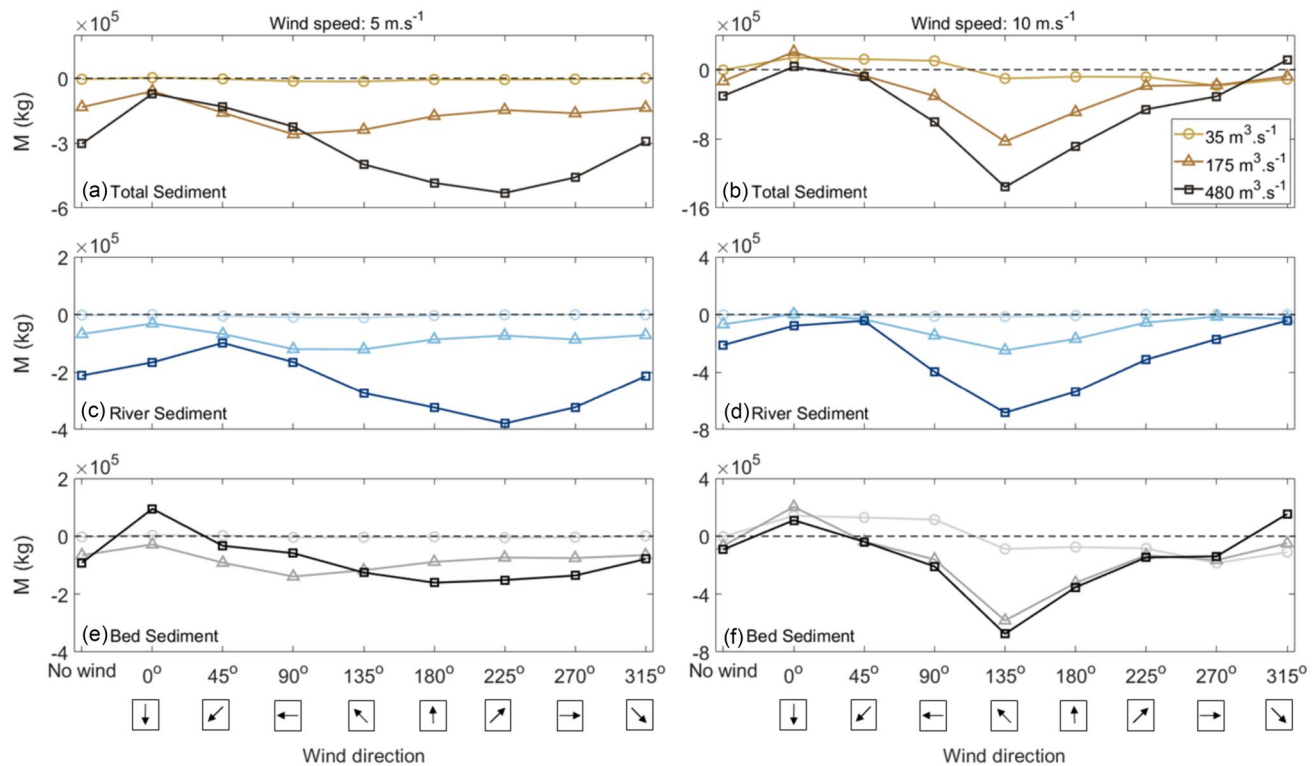


Fig. 9 Comparison of the total (a and b), riverine (c and d), and bed-sourced sediment mass loads in kg (e and f) over the full transect for $35 \text{ m}^3 \text{ s}^{-1}$ (lighter shade, circles), $175 \text{ m}^3 \text{ s}^{-1}$ (triangles), and $480 \text{ m}^3 \text{ s}^{-1}$ (darker shades, squares) discharge scenarios with wind

speeds of 5 m s^{-1} (a, c, and e) and 10 m s^{-1} (b, d, and f). Positive and negative mass loads indicate sediment transport out of the forest and into the forest region, respectively. Arrows in square boxes represent the wind direction

Discussion

In this paper, we used an idealized 3D numerical model to examine the sediment transport patterns resulting from the interaction of a buoyant river plume with mangrove vegetation. In particular, we explored the impact of various forcings (discharges and wind velocities) on the river plume by quantifying sediment fluxes into the forest. The key patterns into and out of the forest are described in terms of the different regions of the river plume (Horner-Devine et al. 2015), and are summarized in Fig. 10. The near-field region of a river plume is defined as an area where estuarine flow is supercritical, and the dynamics are dominated by advection and shear mixing. This region is distinct from the far-field region, where controls are influenced by the earth's rotation, wind, and background flow. It is important to note that the chosen salinity ranges in this study are based on a prior investigation by Vundavilli et al. (2021). The salinity values, in relation to the momentum balances evaluated across different regions of the river plume, aided in classifying its structure.

Sediment Transport within the Different Sections of the River Plume

Near-Field Region

Irrespective of the discharge employed, sediment was deposited inside the forest in the near-field region of the river plume at the river mouth (Figs. 5 and 10a and b). The lateral spreading of sediments and formation of residual currents has been observed in locations without vegetation (see Leonardi et al. (2013), who studied the effects of tides on the evolution of mouth bars). While the directional trends remained similar in the case of non-vegetated simulations, drag from vegetation (particularly during the ebb stage of the tidal cycle), further enhances the deposition of sediment in this near-field forested region.) This deposition is consistent with the satellite images of this rapid progradation of mangroves closer to the river mouth (Fig. 1c). This deposition of sediment near the river mouth was also noted in real-world scenarios, including large rivers like the Amazon (Allison

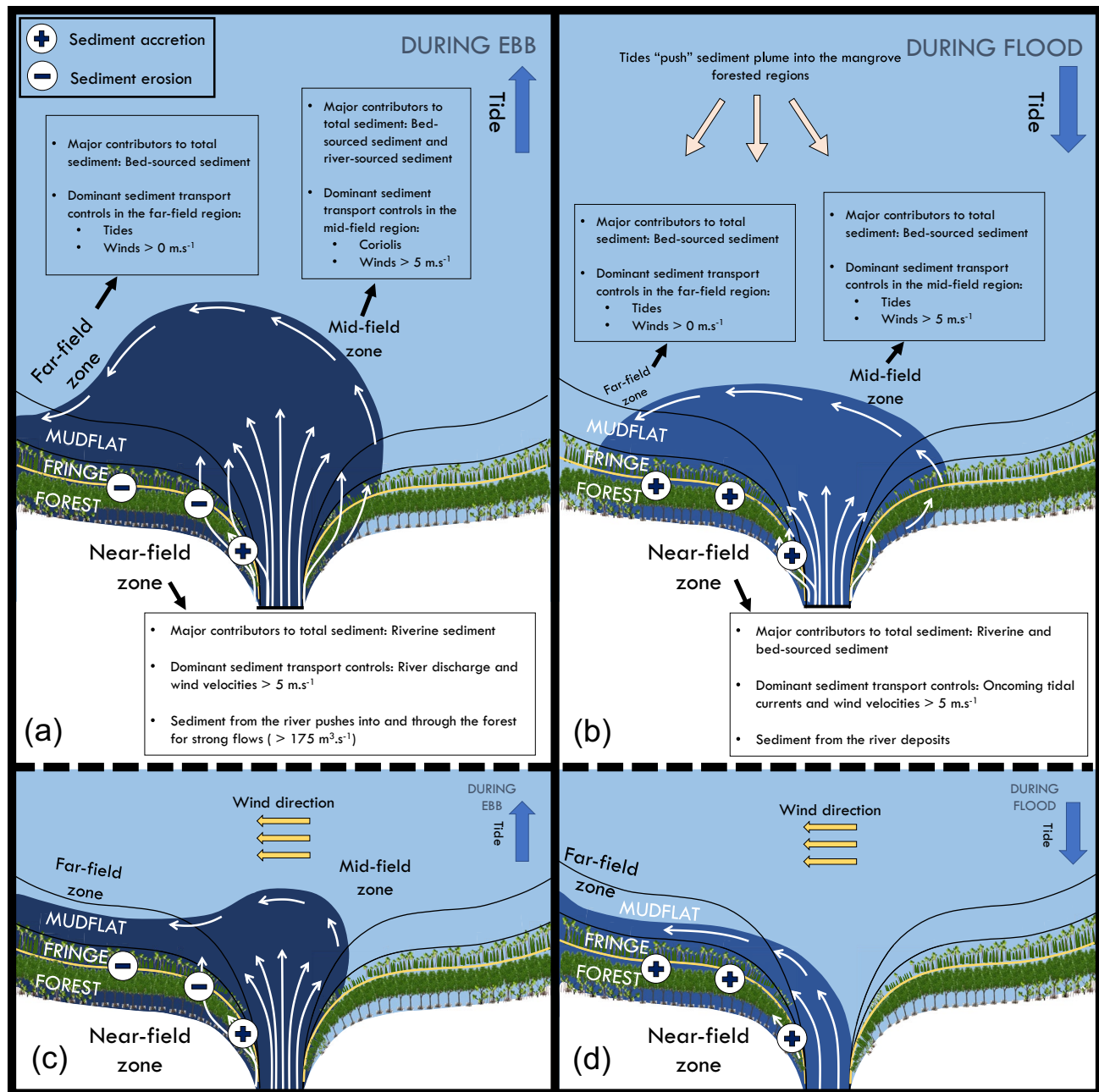


Fig. 10 Panels **a** and **b** depict the extent of the riverine sediment plume during the ebb and flood stages of the tidal cycle, illustrating the diverse dynamics and contributions from external forces to sediment transport mechanisms within different environments of a river plume. Panels **c** and **d** present surface snapshots of an example river

plume during the ebb and flood stages of the tidal cycle under the influence of strong easterly winds. The black arrows in panels **a** and **b** indicate the dominant dynamics within various regions of the river plume during the ebb and flood stages of the tidal cycle, respectively

et al. 1995) and the Yangtze (McKee et al. 1983), where the near-field region spans many kilometers (e.g., approximately 140–200 km for the Amazon River; Lentz (1995)). Similar patterns are also noted in smaller river plumes such as the river Teign (Van Lancker et al. 2004) and the Tseng-wen River (Liu et al. 2002). Along the transect considered in

our study, while flux was landward in the deeper section of the transect, the flux was found to be seaward in the case of shallow regions of the transect (consistent with previous studies such as Ralston et al. (2012) that investigated the effects of bathymetry on sediment transport in the Hudson River estuary).

The relative influences of tides and river varied across our simulations. In low discharge scenarios, the near-field region extended over a few hundred meters out of the river mouth during the ebb stage of the tidal cycle, and this zone disappeared during flood due to the oncoming tidal currents. This formation of the river plume after each tidal cycle has previously been reported in the case of tidally modulated outflow plumes such as River Teign (Pritchard 2000). In the case of large discharges, a persistent plume bulge exists over the entire tidal cycle (Horner-Devine 2009; Jurisa and Chant 2012).

The presence of vegetative drag altered the modeled sediment fluxes in our study. Closer to the river mouth, in the near-field region, as the river debouched into the coastal region, presence of vegetative drag led to reduced velocities, thereby leading to reduced deposition in comparison to non-vegetated simulations. The impact of vegetation varied on the bed-sourced sediment based on the river discharge employed in our model simulations. In particular, while the total sediment fluxes were higher in the presence of vegetation for low discharge runs ($0\text{--}105\text{ m}^3\text{ s}^{-1}$), in the cases of higher discharge ($\geq 140\text{ m}^3\text{ s}^{-1}$), the bed-sourced sediment flux was found to be larger in the case of non-vegetated runs. This difference in trends can be attributed to the impact of the high bottom shear stresses generated by vegetation (see Norris et al. 2021).

Mid-field Region

In the mid-field region (transition region between the near- and far-field region of river plume), a small portion ($\sim 15\%$) of the total sediment delivered by the river in the near-field exited the forest in the case of both the vegetated and non-vegetated model simulations. Additionally, the total sediment fluxes were significantly lower than the magnitudes in the near-field region. Previous studies conducted by Horner-Devine et al. (2015) explained that within the mid-field region, the dominance of Coriolis forces arrests any lateral transport, thereby leading to reduced sediment transport into the mangrove forest.

Dronkers (1986) previously established that concave-up tidal flat profile reduces tidal ranges along with a shorter duration of high water, leading to decreased external sediment supply. In our study, the offshore direction of sediment fluxes noted in the mid-field zone of the river plume can also be explained by the concave-up depth profile in the mid-field region. Furthermore, the tidal asymmetry patterns evaluated in the mid-field region exhibited ebb dominance of the tide. This ebb dominance indicated a mechanism through which the bed-sourced sediment in the shallow regions of the transect was lifted off the bed during the flood stage of the tidal cycle. During the subsequent ebb stage, this bed-sourced sediment was directed away from the forest.

Far-field Region

In the far-field region of the river plume, a comparison of total sediment fluxes between the vegetated and non-vegetated model simulations yielded a reversal of flux direction (directed out of the forest). In particular, while sediment fluxes were found to be directed into the forest in the case of non-vegetated simulation, sediment fluxes in the case of vegetated simulations were instead directed out of the forest (Fig. 10a). This change in flux direction along the edge of the mangrove forest can be attributed to the changes in tidal asymmetry induced by the presence of vegetation (see Bryan et al. 2017; Vundavilli et al. 2021). In the mid- and far-field regions, as the flow is predominantly directed out of the forest, vegetative drag aids in reducing resuspension of sediments.

In our study, when the model is forced with river discharges of $35\text{ m}^3\text{ s}^{-1}$ – $105\text{ m}^3\text{ s}^{-1}$, the riverine momentum is not sufficiently large enough to transfer sediment in the regions away from the river mouth. This reduced riverine sediment in the far-field region was noted in our results (see Figs. 5b and 10a and b), wherein bed-sourced sediment remained the major contributor towards the total sediment transport. The enhanced bed-sourced sediment contribution to the total sediment flux can be attributed to the increased vertical mixing (induced by advective and frontogenetic processes) aided by tides (Ayouché et al. 2020). Furthermore, as expected, the influence of tides reduced as the river discharge increased (Fig. 5b). This result was also reflected in our study: bed-sediment sediment fluxes over the tidal cycle (Fig. 5c) were nearly the same, while the riverine sediment fluxes (Fig. 5b) increased with an increase in river discharge. However, total sediment mass transport in the mid-field region of the plume was reduced for larger river discharges ($> 385\text{ m}^3\text{ s}^{-1}$, Fig. 6a). This reduction was previously explained by Chao (1990), who using modeling techniques found that the presence of tides in an estuarine plume system leads to restriction of plume advection in the cross-shelf direction.

The Influence of Plume Behavior on Sediment Transport

Horizontal advection in a river plume is controlled by plume buoyancy, mixing, and transport (Horner-Devine et al. 2015). Garvine (1995) previously identified limiting cases of offshore plume behavior based on the Kelvin number at the river mouth, defined as the ratio of the source width and the baroclinic deformation radius: $K = W / \left(\frac{\sqrt{g'h}}{f} \right)$, where W is the width of the river mouth g' is the reduced gravity, h is the depth at the river mouth, and f is the Coriolis frequency ($0.875 \times 10^{-4}\text{ s}^{-1}$ at -37° latitude). Plumes with $K \gg 1$ indicate linear dynamics

and exhibit a geostrophic balance in the across-shore directions. Conversely, plumes with $K \ll 1$ demonstrate sharp frontal boundaries and non-linear flow dynamics, while plumes with $K \sim 1$ were classified as intermediate cases.

We evaluated the tidal mean Kelvin numbers inside the river plume at a fixed latitudinal distance of ~ 1 km (Fig. 2a) for our simulations. For flows greater than $385 \text{ m}^3 \text{ s}^{-1}$, the “large” plumes drive enhanced vertical mixing, resulting in smaller g' and Kelvin numbers from ~ 1.2 to ~ 1.35 . In these cases, Coriolis acceleration becomes crucial, and large riverine sediment transport into the forest in the mid- and far-field regions is driven by both plume spreading and rotation dynamics. For the low discharge scenarios ranging from $35 \text{ m}^3 \text{ s}^{-1}$ to $245 \text{ m}^3 \text{ s}^{-1}$, lateral plume spread is restricted, Kelvin numbers were ~ 0.20 to ~ 0.78 (owing to the larger g'), outflow momentum and non-linear terms are more important than rotation, and contributions from riverine sediments to the mangrove forest are smaller than the compared to bed-sourced sediment. Discharges of $280 \text{ m}^3 \text{ s}^{-1}$ – $350 \text{ m}^3 \text{ s}^{-1}$ in our study could be considered intermediate-sized plumes ($0.85 < K < 1.05$).

Furthermore, results from our study align with those from real-world river plumes with similar Kelvin numbers (estimated from the inverse of non-dimensional values given in Crawford 2017), noting that values of K from the discharge scenarios of $35 \text{ m}^3 \text{ s}^{-1}$ and $140 \text{ m}^3 \text{ s}^{-1}$ closely match values estimated for the Rhine River ($K = 0.2$) and the Elbe River ($K \sim 0.5$), respectively. Additionally, Garvine (1995) noted a Kelvin number ~ 1 for the Niagara River plume in Lake Ontario, which dynamically compares to our model simulation with a discharge of $350 \text{ m}^3 \text{ s}^{-1}$.

The Influence of Tides

The spatial extent of the river plume was longer during ebb in comparison to the flood stage due to the oncoming tidal currents. However, the difference between the modeled extents reduced as the discharge employed increased, indicating the reduced impact of tidal modulation of the river plume. Interestingly, the relative tidal modulation and therefore the river plume expansion, was greater in the case of river plumes with the largest discharges ($455 \text{ m}^3 \text{ s}^{-1}$ and $480 \text{ m}^3 \text{ s}^{-1}$) relative to the medium discharges ($280 \text{ m}^3 \text{ s}^{-1}$ – $420 \text{ m}^3 \text{ s}^{-1}$). This enhanced tidal modulation in the case of high discharge regimes was previously observed for the lower Apalachicola River in the Gulf of Mexico, and the effect attributed to the phase change between water level and velocity fluctuations (Leonardi et al. 2015).

The Impact of Wind

The majority of the sediment transport away from the river mouth (in the mid- and far-field region) was dominated by

the direction of the wind, while closer to the river mouth, the plume retained its structure and was less sensitive to winds. For 5 m s^{-1} winds, irrespective of the river discharge, sediment transport was directed into the forest as winds had little to no effect on the near-field region and retained the plume structure in the near-field while forming a bulge. This retention of the plume structure under the influence of weak winds was observed in the case of Changjiang River plume (see Ge et al. 2015). While the dominant sediment loads in the case of smaller and medium discharges were found in the case of easterly winds (perpendicular to the plume), for the large discharges, dominant loads were noted for the westerly winds (particularly southwesterly, 225°) which pushed the plume away from the forest. These enhanced loads in the case of westerly winds can be explained by the reduced sediment outflow in the mid-field region compared to sediment inflow in the near-field region of the river plume. Upon doubling the wind velocities (10 m s^{-1}), plume waters are strongly advected in the downwind direction, and tidal variability within the plume structure is diminished (Fig. 10c and d).

In our model simulations, wind stress was one of the major controlling factors of sediment deposition in the case of small to medium discharge scenarios (Fig. 9). This result is similar to Marques et al. (2009), who studied the dynamics of the Patos Lagoon coastal plume using 3-D numerical experiments and found that while winds become a primary contributor of the transport, the Coriolis force and bed shear stress become secondary influences in the case of low discharge plumes and vice versa. On the other hand, in our model simulations with stronger river flows, a combined influence of Coriolis and bed shear stress (impacted by vegetation) formed the principal dynamical processes controlling the sediment transport.

The presence of winds also played a significant role in altering the Kelvin numbers observed in our study. When winds aligned with the plume direction (135° – 225°), we observed a reduction in Kelvin numbers for both 5 m s^{-1} and 10 m s^{-1} wind speeds. The enhanced lateral dispersion and spreading of the river plume along the mangrove forest resulted in a thinner surface plume and larger g' , which in turn resulted in smaller K values, which were consistent with findings reported by Huq (2009). Conversely, when winds opposed the plume direction, we observed larger Kelvin numbers, indicative of a more concentrated plume with reduced lateral spreading, enhanced mixing, and smaller g' (as noted in (Garvine 1995)). For example, for the scenario with a riverine discharge of $175 \text{ m}^3 \text{ s}^{-1}$ and 10 m s^{-1} winds, Kelvin numbers range from ~ 0.2 to 0.8 for wind directions of 225° and 45° , respectively.

In the case of large discharge scenarios, the presence of strong winds led to the formation of a bidirectional and

thicker plume front in the near-field region of the river plume. This bidirectional plume in our study is evident under the influence of the onshore winds, wherein sediment loads were primarily directed into the forest in the near-field region of the plume. In contrast, sediment transport was directed out of the forest away from the river plume (Fig. 9b). Additionally, under the ebb conditions, as the plume was pushed back into the forest, stronger winds and tides led to enhanced shear stresses on the bottom layer, leading to enhanced bed-sourced sediment transport mass loads in the case of 10 m s^{-1} winds. This alteration to shear stresses in the presence of strong winds is consistent with many studies, such as the Rhine River mouth (Rijnsburger et al. 2018). They attributed this enhanced bed-shear stresses to the increase in strong-return currents in the near-bed layer, which results from the fast and thick plume fronts.

Lastly, within the river plume, wind-induced shear at the surface layer altered the flow patterns in the vertical water column in the case of low discharge scenarios ($35 \text{ m}^3 \text{ s}^{-1}$ – $140 \text{ m}^3 \text{ s}^{-1}$). However, in the case of large discharge scenarios, flow reversal occurred only in the presence of strong winds (speeds $> 5 \text{ m s}^{-1}$, also noted by García Berdeal et al. 2002) as the induced wind stress is not sufficiently large to overcome the ambient flow closer to the river mouth.

Conclusions

Sediment transport patterns within a mangrove forest are altered by the interaction of fluvial, estuarine, and marine processes. This idealized model study offers insights into how discharge and winds influence sediment transport in a mangrove river plume. However, our study does not incorporate the impact of wind waves on overall sediment transport patterns. Representing the presence of mangrove trees and roots using bottom drag enables us to capture these critical feedback mechanisms within the mangroves with higher computational efficiency (Horstman et al. 2015); however, a detailed understanding of the modifications to the turbulent fields obtained using vegetative stems is neglected. The present study also neglects flocculation processes, noting that floc size has been shown to vary substantially along tidal rivers (MacDonald and Mullarney 2015). Future research could address these aspects for a more comprehensive understanding.

Funding Acknowledgment is made to the donors of the American Chemical Society Petroleum Research fund for support of this research (Grant number PRF #56786-ND8).

Data Availability Data will be made available on request.

Declarations

Competing Interests Authors declare no competing interests.

Open Access This article is licensed under a Creative Commons Attribution 4.0 International License, which permits use, sharing, adaptation, distribution and reproduction in any medium or format, as long as you give appropriate credit to the original author(s) and the source, provide a link to the Creative Commons licence, and indicate if changes were made. The images or other third party material in this article are included in the article's Creative Commons licence, unless indicated otherwise in a credit line to the material. If material is not included in the article's Creative Commons licence and your intended use is not permitted by statutory regulation or exceeds the permitted use, you will need to obtain permission directly from the copyright holder. To view a copy of this licence, visit <http://creativecommons.org/licenses/by/4.0/>.

References

- Allison, M., C. Nittrouer, and L.D.C. Faria Jr. 1995. Rates and mechanisms of shoreface progradation and retreat downdrift of the Amazon River mouth. *Marine Geology* 125 (3–4): 373–392.
- Ayouche, A., X. Carton, G. Charria, S. Theetten, and N. Ayoub. 2020. Instabilities and vertical mixing in river plumes: application to the Bay of Biscay. *Geophysical & Astrophysical Fluid Dynamics* 114 (4–5): 650–689.
- Balke, T., T.J. Bouma, E.M. Horstman, E.L. Webb, P.L. Erftemeijer, and P.M. Herman. 2011. Windows of opportunity: thresholds to mangrove seedling establishment on tidal flats. *Marine Ecology Progress Series* 440: 1–9.
- Balke, T., T. Bouma, P. Herman, E. Horstman, C. Sudtongkong, and E. Webb. 2013. Cross-shore gradients of physical disturbance in mangroves: Implications for seedling establishment. *Biogeosciences* 10 (8): 5411–5419.
- Baptist, M. 2005. *Modelling floodplain biogeomorphology*. PhD thesis, The Faculty of Civil Engineering and Geosciences, Delft University of Technology, Delft, Netherlands.
- Barbier, E.B., S.D. Hacker, C. Kennedy, E.W. Koch, A.C. Stier, and B.R. Silliman. 2011. The value of estuarine and coastal ecosystem services. *Ecological Monographs* 81 (2): 169–193.
- Bryan, K.R., W. Nardin, J.C. Mullarney, and S. Fagherazzi. 2017. The role of cross-shore tidal dynamics in controlling intertidal sediment exchange in mangroves in Cù Lao Dung, Vietnam. *Continental Shelf Research* 147: 128–143.
- Chao, S.Y. 1988a. River-forced estuarine plumes. *Journal of Physical Oceanography* 18 (1): 72–88.
- Chao, S.Y. 1988b. Wind-driven motion of estuarine plumes. *Journal of Physical Oceanography* 18 (8): 1144–1166.
- Chao, S.Y. 1990. Tidal modulation of estuarine plumes. *Journal of Physical Oceanography* 20 (7): 1115–1123.
- Chen, F., D.G. MacDonald, and R.D. Hetland. 2009. Lateral spreading of a near-field river plume: observations and numerical simulations. *Journal of Geophysical Research* 114: C07013.
- Chen, Z., A. Ortiz, L. Zong, and H. Nepf. 2012. The wake structure behind a porous obstruction and its implications for deposition near a finite patch of emergent vegetation. *Water Resources Research* 48: 1–12. <https://doi.org/10.1029/2012WR012224>.
- Crawford, T.J. 2017. *An experimental study of the spread of buoyant water into a rotating environment*. Ph. D. thesis, University of Cambridge.

- Deltares. 2021. Delft3D-Flow, Simulation of multi-dimensional hydrodynamic flows and transport phenomena, including sediments, User Manual, Version 3.15.34158, May 2021, 684 pp.
- Dronkers, J. 1986. Tidal asymmetry and estuarine morphology. *Netherlands Journal of Sea Research* 20 (2–3): 117–131.
- Fricke, A., C. Nittrouer, A. Ogston, and H. Vo-Luong. 2017. Asymmetric progradation of a coastal mangrove forest controlled by combined fluvial and marine influence, Cù Lao Dung, Vietnam. *Continental Shelf Research* 147: 78–90.
- Furukawa, K., and E. Wolanski. 1996. Sedimentation in mangrove forests. *Mangroves and Salt marshes* 1 (1): 3–10.
- García Berdeal, I., B. Hickey, and M. Kawase. 2002. Influence of wind stress and ambient flow on a high discharge river plume. *Journal of Geophysical Research: Oceans* 107 (C9): 13–1.
- Garvine, R.W. 1987. Estuary plumes and fronts in shelf waters: A layer model. *Journal of Physical Oceanography* 17 (11): 1877–1896.
- Garvine, R.W. 1995. A dynamical system for classifying buoyant coastal discharges. *Continental Shelf Research* 15 (13): 1585–1596.
- Ge, J., P. Ding, and C. Chen. 2015. Low-salinity plume detachment under non-uniform summer wind off the Changjiang Estuary. *Estuarine, Coastal and Shelf Science* 156: 61–70.
- Giri, C., E. Ochieng, L.L. Tieszen, Z. Zhu, A. Singh, T. Loveland, J. Masek, and N. Duke. 2011. Status and distribution of mangrove forests of the world using earth observation satellite data. *Global Ecology and Biogeography* 20 (1): 154–159.
- Henderson, S.M., B.K. Norris, J.C. Mullarney, and K.R. Bryan. 2017. Wave-frequency flows within a near-bed vegetation canopy. *Continental Shelf Research* 147: 91–101.
- Hetland, R.D. 2005. Relating river plume structure to vertical mixing. *Journal of Physical Oceanography* 35 (9): 1667–1688.
- Horner-Devine, A.R. 2009. The bulge circulation in the Columbia River plume. *Continental Shelf Research* 29 (1): 234–251.
- Horner-Devine, A.R., R.D. Hetland, and D.G. MacDonald. 2015. Mixing and transport in coastal river plumes. *Annual Review of Fluid Mechanics* 47: 569–594.
- Horstman, E.M., C.M. Dohmen-Janssen, and S.J.M.H. Hulscher. 2013. Modeling tidal dynamics in a mangrove creek catchment in Delft3D. *Coastal Dynamics Proceedings* 2013: 833–844.
- Horstman, E.M., C.M. Dohmen-Janssen, T.J. Bouma, and S.J. Hulscher. 2015. Tidal-scale flow routing and sedimentation in mangrove forests: Combining field data and numerical modelling. *Geomorphology* 228: 244–262.
- Horstman, E.M., C.J. Lundquist, K.R. Bryan, R.H. Bulmer, J.C. Mullarney, and D.J. Stokes. 2018. *The dynamics of expanding mangroves in New Zealand, Threats to Mangrove Forests*, 23–51. Springer.
- Huq, P. 2009. The role of kelvin number on bulge formation from estuarine buoyant outflows. *Estuaries and Coasts* 32: 709–719.
- Jurisa, J.T., and R. Chant. 2012. The coupled Hudson River estuarine-plume response to variable wind and river forcings. *Ocean Dynamics* 62 (5): 771–784.
- Kumara, M., L. Jayatissa, K. Krauss, D. Phillips, and M. Huxham. 2010. High mangrove density enhances surface accretion, surface elevation change, and tree survival in coastal areas susceptible to sea-level rise. *Oecologia* 164 (2): 545–553.
- Lentz, S.J. 1995. Seasonal variations in the horizontal structure of the Amazon Plume inferred from historical hydrographic data. *Journal of Geophysical Research: Oceans* 100 (C2): 2391–2400.
- Leonardi, N., A. Canestrelli, T. Sun, and S. Fagherazzi. 2013. Effect of tides on mouth bar morphology and hydrodynamics. *Journal of Geophysical Research: Oceans* 118 (9): 4169–4183.
- Leonardi, N., A.S. Kolker, and S. Fagherazzi. 2015. Interplay between river discharge and tides in a delta distributary. *Advances in Water Resources* 80: 69–78.
- Lesser, G.R., J.V. Roelvink, J. Van Kester, and G. Stelling. 2004. Development and validation of a three-dimensional morphological model. *Coastal Engineering* 51 (8–9): 883–915.
- Li, L., X.H. Wang, F. Andutta, and D. Williams. 2014. Effects of mangroves and tidal flats on suspended-sediment dynamics: Observational and numerical study of Darwin Harbour. *Australia. Journal of Geophysical Research: Oceans* 119 (9): 5854–5873.
- Liu, J.T., S.Y. Chao, and R.T. Hsu. 2002. Numerical modeling study of sediment dispersal by a river plume. *Continental Shelf Research* 22 (11–13): 1745–1773.
- Lovelock, C.E., D.R. Cahoon, D.A. Friess, G.R. Guntenspergen, K.W. Krauss, R. Reef, K. Rogers, M.L. Saunders, F. Sidik, A. Swales, et al. 2015. The vulnerability of Indo-Pacific mangrove forests to sea-level rise. *Nature* 526 (7574): 559–563.
- MacDonald, I.T., and J.C. Mullarney. 2015. A novel “FlocDrifter” platform for observing flocculation and turbulence processes in a Lagrangian frame of reference. *Journal of Atmospheric and Oceanic Technology* 32 (3): 547–561.
- Marques, W., E. Fernandes, I. Monteiro, and O. Möller. 2009. Numerical modeling of the Patos Lagoon coastal plume, Brazil. *Continental Shelf Research* 29 (3): 556–571.
- Mazda, Y., N. Kanazawa, and E. Wolanski. 1995. Tidal asymmetry in mangrove creeks. *Hydrobiologia* 295 (1): 51–58.
- Mazda, Y., E. Wolanski, B. King, A. Sase, D. Ohtsuka, and M. Magi. 1997. Drag force due to vegetation in mangrove swamps. *Mangroves and Salt Marshes* 1 (3): 193–199.
- Mazda, Y., M. Magi, Y. Ikeda, T. Kurokawa, and T. Asano. 2006. Wave reduction in a mangrove forest dominated by *Sonneratia* sp. *Wetlands Ecology and Management* 14 (4): 365–378.
- Mazzini, P.L., and R.J. Chant. 2016. Two-dimensional circulation and mixing in the far field of a surface-advected river plume. *Journal of Geophysical Research: Oceans* 121 (6): 3757–3776.
- McCabe, R.M., B.M. Hickey, and P. MacCready. 2008. Observational estimates of entrainment and vertical salt flux in the interior of a spreading river plume. *Journal of Geophysical Research* 113: C08027.
- McKee, B.A., C.A. Nittrouer, and D.J. DeMaster. 1983. Concepts of sediment deposition and accumulation applied to the continental shelf near the mouth of the Yangtze River. *Geology* 11 (11): 631–633.
- Mehta, A.J., and E. Partheniades. 1982. Resuspension of deposited cohesive sediment beds. *Coastal Engineering* 1982: 1569–1588.
- Montgomery, J.M., K.R. Bryan, J.C. Mullarney, and E.M. Horstman. 2019. Attenuation of storm surges by coastal mangroves. *Geophysical Research Letters* 46 (5): 2680–2689.
- Mullarney, J.C., S.M. Henderson, B.K. Norris, K.R. Bryan, A.T. Fricke, D.R. Sandwell, and D.P. Culling. 2017. A question of scale: How turbulence around aerial roots shapes the seabed morphology in mangrove forests of the Mekong Delta. *Oceanography* 30 (3): 34–47.
- Mullarney, J.C., S.M. Henderson, J.A. Reyns, B.K. Norris, and K.R. Bryan. 2017. Spatially varying drag within a wave-exposed mangrove forest and on the adjacent tidal flat. *Continental Shelf Research* 147: 102–113.
- Nepf, H. 2004. *Vegetated flow dynamics*, 137–163. Washington, DC: The Ecogeomorphology of Tidal Marshes. American Geophysical Union.
- Nepf, H.M. 2012. Flow and transport in regions with aquatic vegetation. *Annual Review of Fluid Mechanics* 44: 123–142.
- Nittrouer, C.A., G.J. Brunskill, and A.G. Figueiredo. 1995. Importance of tropical coastal environments. *Geo-Marine Letters* 15 (3–4): 121–126.
- Norris, B.K., J.C. Mullarney, K.R. Bryan, and S.M. Henderson. 2017. The effect of pneumatophore density on turbulence: A field study in a *Sonneratia*-dominated mangrove forest, Vietnam. *Continental Shelf Research* 147: 114–127.

- Norris, B.K., J.C. Mullarney, K.R. Bryan, and S.M. Henderson. 2019. Turbulence within natural mangrove pneumatophore canopies. *Journal of Geophysical Research: Oceans* 124 (4): 2263–2288.
- Norris, B.K., J.C. Mullarney, K.R. Bryan, and S.M. Henderson. 2021. Relating millimeter-scale turbulence to meter-scale subtidal erosion and accretion across the fringe of a coastal mangrove forest. *Earth Surface Processes and Landforms* 46 (3): 573–592.
- Oorschot, M.V., M. Kleinhans, G. Geerling, and H. Middelkoop. 2016. Distinct patterns of interaction between vegetation and morphodynamics. *Earth Surface Processes and Landforms* 41 (6): 791–808.
- Pritchard, Mark. 2000. Dynamics of a small tidal estuarine plume. Plymouth, England: The University of Plymouth, Doctoral thesis, 173 pp.
- Ralston, D.K., W.R. Geyer, and J.C. Warner. 2012. Bathymetric controls on sediment transport in the Hudson River estuary: Lateral asymmetry and frontal trapping. *Journal of Geophysical Research* 117: C10013. <https://doi.org/10.1002/2013JGL057906>.
- Rijnsburger, S., R.P. Flores, J.D. Pietrzak, A.R. Horner-Devine, and A.J. Souza. 2018. The influence of tide and wind on the propagation of fronts in a shallow river plume. *Journal of Geophysical Research: Oceans* 123 (8): 5426–5442.
- Roelvink, J., and G. Van Banning. 1995. Design and development of Delft3D and application to coastal morphodynamics. *Oceanographic Literature Review* 11 (42): 925.
- Sheaves, M., R. Baker, I. Nagelkerken, and R.M. Connolly. 2015. True value of estuarine and coastal nurseries for fish: Incorporating complexity and dynamics. *Estuaries and Coasts* 38 (2): 401–414.
- Temmerman, S., T. Bouma, J. Van de Koppel, D. Van der Wal, M. De Vries, and P. Herman. 2007. Vegetation causes channel erosion in a tidal landscape. *Geology* 35 (7): 631–634.
- Van Lancker, V., J. Lanckneus, S. Hearn, P. Hoekstra, F. Levoy, J. Miles, G. Moerkerke, O. Monfort, and R. Whitehouse. 2004. Coastal and nearshore morphology, bedforms and sediment transport pathways at Teignmouth (UK). *Continental Shelf Research* 24 (11): 1171–1202.
- Vundavilli, H., J.C. Mullarney, I.T. MacDonald, and K.R. Bryan. 2021. The interaction of buoyant coastal river plumes with mangrove vegetation and consequences for sediment deposition and erosion in a tidal environment. *Continental Shelf Research* 222: 104417.
- Walsh, J., and C. Nittrouer. 2004. Mangrove-bank sedimentation in a mesotidal environment with large sediment supply, Gulf of Papua. *Marine Geology* 208 (2–4): 225–248.
- Wolanski, E., S. Spagnol, and E.B. Lim. 2002. Chapter eleven fine sediment dynamics in the mangrove-fringed, muddy coastal zone. In *Proceedings in Marine Science*, vol. 4, 279–292. Elsevier.
- Woodroffe, C. 1992. Mangrove sediments and geomorphology. In *Tropical Mangrove Ecosystems*, vol. 41, 7–41. American Geophysical Union.
- Zhang, K., H. Liu, Y. Li, H. Xu, J. Shen, J. Rhome, and T.J. Smith III. 2012. The role of mangroves in attenuating storm surges. *Estuarine, Coastal and Shelf Science* 102: 11–23.
- Zong, L., and H. Nepf. 2012. Vortex development behind a finite porous obstruction in a channel. *Journal of Fluid Mechanics* 691: 368–391.